



## ARTICLE

DOI: 10.1038/s42005-018-0065-9

OPEN

# Multiple self-healing Bloch surface wave beams generated by a two-dimensional fraxicon

Myun-Sik Kim <sup>1</sup>, Andreas Vetter <sup>2,3</sup>, Carsten Rockstuhl<sup>2,4</sup>, Babak Vosoughi Lahijani<sup>1</sup>, Markus Häyriinen<sup>5</sup>, Markku Kuittinen<sup>5</sup>, Matthieu Roussey<sup>5</sup> & Hans Peter Herzig<sup>1</sup>

Two-dimensional surface waves are a cornerstone for future integrated photonic circuits. They can also be beneficially exploited in sensing devices by offering dark-field illuminations of objects. One major problem in sensing schemes arises from the individual sensing objects: the interaction of surface waves with an object reduces the field amplitude, and the readout of other objects along the propagation path suffers from this reduced signal. Here we show in two experiments that nondiffracting and self-healing Bloch surface waves can be launched using a Fresnel axicon (i.e., fraxicon). First, we visualize the generation of an array of multiple focal spots by scanning near-field optical microscopy in the infrared. With a second device operating in the visible, we demonstrate the self-healing effect directly using a far-field readout method by placing metallic nanoantennas onto the multiple focal spots of the fraxicon. Our study extends the versatile illumination capabilities of surface wave systems.

<sup>1</sup>Optics & Photonics Technology Laboratory, Ecole Polytechnique Fédérale de Lausanne (EPFL), Neuchâtel CH-2002, Switzerland. <sup>2</sup>Institute of Nanotechnology, Karlsruhe Institute of Technology, 76344 Eggenstein-Leopoldshafen, Germany. <sup>3</sup>SUSS MicroOptics SA, Rogues-Terres 61, Hauterive CH 2068, Switzerland. <sup>4</sup>Institute of Theoretical Solid State Physics, Karlsruhe Institute of Technology, 76131 Karlsruhe, Germany. <sup>5</sup>Institute of Photonics, University of Eastern Finland, P.O. Box 11180101 Joensuu, Finland. These authors contributed equally: Myun-Sik Kim, Andreas Vetter. Correspondence and requests for materials should be addressed to M.-S.K. (email: [myunsik@hotmail.com](mailto:myunsik@hotmail.com))

Two-dimensional (2D) surface wave devices have been demonstrated for a variety of applications in the realm of miniaturized optical systems<sup>1–4</sup>. They are appealing as they offer strong field confinement at the interface between the device surface and the external medium. Especially in the context of sensing devices, a multitude of surface wave components for focusing and beam steering have been intensively investigated<sup>5,6</sup>.

Bloch surface waves (BSWs) are a particularly important type of surface waves as they offer a long propagation length and can easily be manipulated in their propagation characteristics. Particularly, the first aspect makes BSWs distinct compared to other surface waves such as surface plasmon polariton (SPP). SPPs are sustained at the interface between a dielectric and a metal and usually have a limited propagation length due to absorption in the metal<sup>7,8</sup>. BSWs are supported by a dielectric multilayer serving as a one-dimensional (1D) photonic crystal (PC)<sup>9</sup>. For one half space, the band-gap of the 1D PC forbids propagation into the multilayer structure, because the frequency of a BSW is located within the photonic band-gap. In the other half space, the field will also be evanescent because the propagation constant of the BSW will be outside the light cone of the outer medium. By placing an additional layer on top of the 1D PC, called the element layer, the propagation and dispersion of the BSWs can be manipulated by choosing a suitable thickness and selecting a proper material with a given permittivity. The finiteness of the multilayer structure causes some radiation losses in the experiments. However, a spurious radiation loss is also essential as it allows the excitation of BSWs via frustrated total internal reflection in the Kretschmann configuration<sup>10</sup>.

Isotropic dielectric media support BSWs. Thus, a wide range of materials are available and various ambient media can be applied. Over the past decade, different BSW platforms have been established in the visible<sup>11,12</sup>, near-infrared (IR)<sup>13–19</sup>, and mid-IR<sup>20</sup> spectral ranges. The lossless dielectric media ensure a long propagation length compared to SPPs. As an example, a propagation length of 3.24 mm for a BSW at a wavelength of 1558 nm was experimentally demonstrated<sup>13</sup>.

Thanks to these promising characteristics of BSWs, numerous researches have been inspired in recent years. For instance, many possibilities for beam manipulation of the propagating BSWs are investigated, e.g., a prism for the refraction effect of the BSW<sup>14</sup>, waveguide components<sup>15–17</sup>, a plano-convex lens<sup>18</sup>, and a photonic nanojet focuser<sup>19</sup>. All these devices are realized by spatially patterning the element layer. The patterned element layer leads to local changes of the dispersion relation of the BSW which controls the way it propagates by a contrast in the effective refractive index. More sophisticated devices, such as linear<sup>11,21</sup> and circular<sup>12</sup> grating couplers, disk resonators<sup>22–24</sup>, a gradient index Luneburg lens<sup>25</sup>, a nanofiber for 1D confinement<sup>26</sup>, BSW polariton devices<sup>27,28</sup>, and subwavelength grooves for the magnetic spin-orbit interaction<sup>29</sup>, have been already demonstrated. Recent research has stretched the application of BSW devices for fluorescence detection<sup>12</sup>, for bio and chemical sensing<sup>30–33</sup>, and to control the properties of surface plasmons<sup>34,35</sup>.

In the in-plane illumination scheme of surface waves, there is, however, a fundamental drawback: any small object, e.g., specimens under test, located in the propagation path of surface waves behaves as an obstacle. Therefore, the incidence surface wave is scattered out of the plane and the surface wave after the object is substantially weakened and perturbed. This prohibits the surface wave to reach the spatial domain behind the object. The 2D nondiffracting surface waves, which resemble Bessel beams<sup>36</sup> in three-dimensional (3D) space, can mitigate this issue and have been recently demonstrated by using crossed grating couplers for SPPs<sup>37</sup> and BSWs<sup>38</sup>. In SPP devices, other components, such as

stripe launchers<sup>39</sup> and a 2D axicon<sup>40</sup>, have also been investigated for the generation of nondiffracting surface waves.

We look here on the problem from a different perspective and highlight the merit of a spread of multiple beams. When generated in a controlled manner with self-healing properties, such multiple beams are perfectly suited for addressing distributed objects. Manifold applications are within reach, such as simultaneous sensing and optical trapping of multiple specimens at different locations. We here take advantage of the concept of a nondiffracting self-healing beam which can be generated by an axicon lens<sup>41</sup>. While axicons produce a single nondiffracting beam, the generation of multiple beams can be obtained by applying the notion of a Fresnel lens to an axicon, termed fraxicon<sup>42</sup>. Fraxicons generate multiple on-axis nondiffracting beams in 3D space which are formed by constructive and destructive interference along the optical axis.

In this contribution we adapt the fraxicon concept to the BSW platform with the purpose to generate multiple self-healing BSW beams. To directly image the self-healing BSW in our work, we conduct initial experiments with suitably designed samples at near-infrared wavelengths, where our scanning near-field optical microscope (SNOM) operates. To probe the ability of the BSW to be restored after interaction with obstacles, we conduct a second set of experiments at visible wavelengths with a suitably designed plasmonic nanoantenna array for a simultaneous readout of multiple spots in the far-field. This hybrid device concept can be extended for more complex manipulations of the BSW using 2D diffractive optical elements or meta-structures.

## Results

**Experimental setup for prism coupling.** The experiments described in this study are based on a Kretschmann configuration<sup>10</sup> for surface wave excitation via frustrated total internal reflection. The schematic of our experimental setup is shown in Fig. 1a, which includes multilayer structures, a fraxicon element, a prism coupler, and a fiber SNOM probe. For near-field investigations, we use the BSW multilayers optimally designed for the SNOM operating wavelength at  $\lambda = 1555$  nm, where the fraxicon element is made of a 47 nm  $\text{TiO}_2$  layer. For the demonstration of simultaneous triggering of an array of gold nanoantennas, we design multilayers for  $\lambda = 660$  nm in order to obtain an enhanced response of the gold nanoantennas and to allow the far-field readout under a standard optical microscope. For this wavelength, the fraxicon is made of 30 nm  $\text{Si}_3\text{N}_4$  layer, depicted in the device schematic on the prism coupling setup in Fig. 1b.

**Near-field investigation of 2D fraxicon at  $\lambda = 1555$  nm.** To characterize a fraxicon device, we first describe its operating principle, which can be explained in analogy to an axicon. The schematics and working principles of axicon and fraxicon devices are shown in Fig. 2. A 2D axicon device has a form of an isosceles triangle as a cross-section of a 3D axicon, which has a form of a conical prism (see Fig. 2a, b). By applying the concept of a Fresnel lens on the axicon device, we can obtain a fraxicon. The cross-section of the 3D fraxicon leads to the 2D fraxicon that consists of two arrays of right-triangular segments touching in the middle (see the device schematics in Fig. 2c, d).

The way an axicon produces a nondiffracting beam relies on the interference effect of two tilted waves, i.e., refracted waves emerging from the slopes of each side. The overlap area of these two tilted waves forms a diamond shape as highlighted by a red diamond in Fig. 2b. Under normal incidence, the incidence angle to the slope  $\theta_i$  equals the base angle  $\theta_b$ , i.e.,  $\theta_i = \theta_b$ . Snell's law leads to the refraction angle  $\theta_r$  of the refracted beams emerging

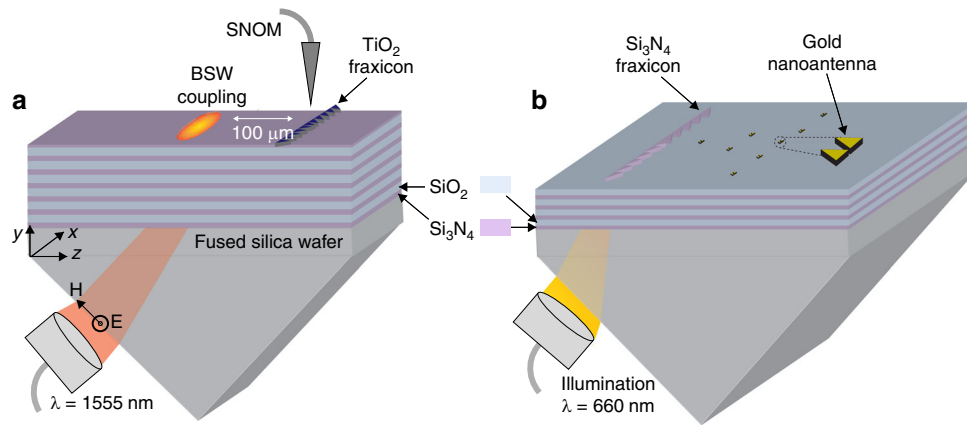


**Fig. 1** Experimental setup. **a** Schematic of the scanning near-field microscope (SNOM) measurement at  $\lambda = 1555$  nm including the multilayer structure, Kretschmann coupling configuration, and the fraxicon device made of a 47 nm  $\text{TiO}_2$  element layer. Bloch surface wave (BSW) is excited 100  $\mu\text{m}$  away from the fraxicon. **b** Schematic of the hybrid surface wave device for  $\lambda = 660$  nm which combines the 2D BSW fraxicon for the illumination and an array of gold nanoantennas for a far-field readout

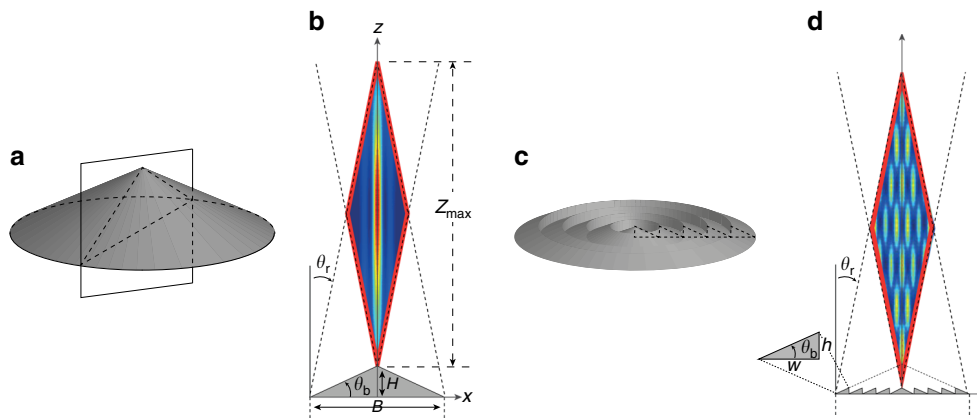


**Fig. 2** Schematics of axicon and fraxicon devices. **a** A 3D axicon (i.e., a conical prism) and **b** its cross-section leading to a 2D axicon, where  $Z_{\text{max}}$  is the maximum propagation distance of a nondiffracting beam,  $\theta_b$  the base angle of the axicon,  $\theta_r$  the refraction angle of the refracted beam emerging from the axicon,  $H$  the height of the axicon, and  $B$  the base length of the axicon. Here, the effective work space of the axicon is the overlap of two refracted waves emerging from each slope of the isosceles triangle (see the red diamond). When the concept of a Fresnel lens is applied to the axicon, **c** a 3D fraxicon is formed by concentric conical rings and **d** its cross-section leading to a 2D fraxicon. Within the diamond work space, exemplary intensity distributions of each device are presented

from the slopes of the axicon,

$$\theta_r = \sin^{-1}\left(\sin \theta_b \frac{n_1}{n_2}\right) - \theta_b, \quad (1)$$

where  $n_1$  and  $n_2$  are the refractive indices of the axicon and the surrounding medium, respectively. The maximum propagation distance  $Z_{\text{max}}$  is defined by the major axis length of the diamond-shaped work space,

$$Z_{\text{max}} = B / (2 \tan \theta_r). \quad (2)$$

$Z_{\text{max}}$  can be controlled by the base length  $B$  and base angle  $\theta_b$  of axicon devices, which vary the size of the diamond-shaped work space. For instance, while the height  $H$  of the axicon is kept constant, a larger  $B$  leads to a smaller  $\theta_r$  and a longer propagation distance  $Z_{\text{max}}$ . This modus operandi is adapted for the fraxicon device, as shown in Fig. 2d. When a plane wave illuminates a 3D fraxicon, it generates multiple on-axis bright spots periodically separated by dark zones<sup>42</sup>. For a 2D fraxicon, the array of micron-size sub-segments leads to diffraction of light as a grating

device, which spreads the incidence wave in space and generates 2D patterns of bright spots. Similar to the axicon, the overlap of two tilted waves is the key for the self-healing properties. Therefore, the lateral extension of the fraxicon and the base angle define the diamond-shaped work space the same as the axicon. Since the lateral extension of the BSWs can be enlarged by a large incident beam without hindering a long propagation length, the scalability of 2D fraxicon devices on the BSW platforms is not fundamentally limited. For the commodity of experiments, we employ here a finite-sized fraxicon device to obtain finitely localized work space of self-healing beams.

For the design parameter variations, we apply a 2D simulation method (see details in Methods section). The device architecture with the multilayer and the 2D fraxicon made of  $\text{TiO}_2$  for  $\lambda = 1555$  nm is shown in Fig. 1a. It is found that a moderate refraction angle  $\theta_r$  tends to generate uniform and an axially symmetric beam shape. When the refraction angle is too large or too small, the nondiffracting beams start to converge or diverge, respectively. The main reason is that the diffraction at edges of a small-size (i.e., micron-size) element is strong enough to break the

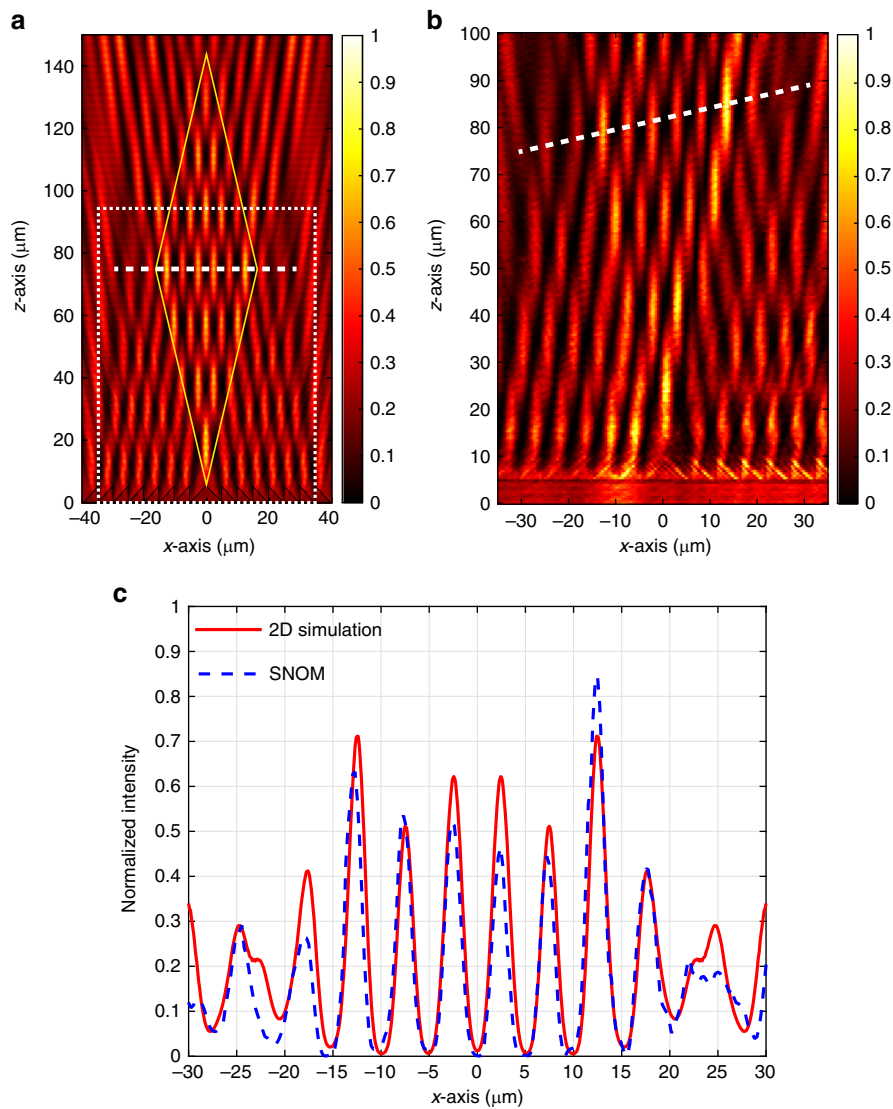


**Fig. 3** Intensity distribution of the fraxicon in the  $x$ - $z$  plane. **a** The result of the 2D simulation and **b** the near-field measurement using a custom-made scanning near-field optical microscope (SNOM) at  $\lambda = 1555$  nm. The designed fraxicon consists of two arrays of eight right triangles ( $w = h = 5$   $\mu\text{m}$ ) meeting at  $x = 0$   $\mu\text{m}$ . Since the maximum scanning range of the SNOM is 100  $\mu\text{m}$ , the measurement window is reduced accordingly, covering approximately an extent of 90  $\mu\text{m}$  behind the fraxicon (see the white dotted box in **(a)**). Imperfection of the collimation and a minor alignment error in the SNOM measurements caused a tilt of 15° of the propagation axis with respect to the reference  $x$ - $z$  coordinate system in **(b)**. **c** The extracted transverse intensity profiles over six spots are marked by white dashed lines in **(a, b)**

symmetric beam pattern of the two-beam interference. The optimal design is obtained for  $\theta_r$  around 5°, i.e., when the base angle  $\theta_b$  equals 45°. The fraxicon consists of two arrays of eight right triangles touching in the middle, i.e.,  $x = 0$   $\mu\text{m}$ , where each segment of the right triangle has dimensions of width ( $w$ ) = height ( $h$ ) = 5  $\mu\text{m}$ , resulting in  $\theta_b = 45^\circ$ . It leads to a size of the complete device of 80  $\mu\text{m}$  in  $x$  and 5  $\mu\text{m}$  in  $z$ -direction. Figure 3a shows the simulated intensity ( $|E_x|^2 + |E_z|^2$ ) distribution behind the fraxicon using the 2D simulation, where the designed fraxicon is depicted in the bottom, i.e.,  $z = 0$  to 5  $\mu\text{m}$ . As expected, multiple self-healing spots are populated within the diamond-shaped work space depicted by yellow solid lines. For the experimental verification, the fabricated fraxicon on the 1555 nm multilayer platform is characterized by the SNOM. A collimated transverse electric (TE)-polarized beam of  $\lambda = 1555$  nm is used as illumination at the excitation angle for the BSW,  $\theta = 56.4^\circ$  inside the glass prism. The custom-made SNOM is equipped with a

metal-coated fiber tip with an aperture size of 200 nm and scans over the device area. Since the maximum scanning range of the SNOM is 100  $\mu\text{m}$ , we set the measurement window to the bottom half of the diamond-shaped work space as depicted by a white dotted rectangle in Fig. 3a. The measured near-field intensity distribution in Fig. 3b demonstrates the generation of multiple self-healing beams.

Along the optical axis, i.e., the  $z$ -axis at  $x = 0$   $\mu\text{m}$ , in Fig. 3a, b, the main feature of the fraxicon is well demonstrated by on-axis bright spots periodically separated by dark zones. As anticipated for the 2D optical system, there are also more spots emerging outside the optical axis. In 3D systems, the rotational symmetry tends to concentrate the incidence wave only on the optical axis. In contrast, the merit of 2D systems emerges by distributing the incident light also out of the optical axis. For the quantitative comparison, we extract transverse intensity profiles along six spots, as depicted by white dashed lines in Fig. 3a, b. These

transverse intensity profiles are plotted together in Fig. 3c. Imperfection of the collimation and a minor alignment error in the SNOM measurement caused a tilt of  $15^\circ$  of the propagation axis with respect to the reference  $x$ - $z$  coordinate system. To compensate this tilt error, the SNOM intensity profile is scaled by  $\cos 15^\circ$ , and afterward it is laterally shifted to overlap with the simulation result. Except small deviations of the peak intensity of each spot, which are caused by aforementioned experimental errors, the measured SNOM data agree very well with the 2D simulation result, proving the validity of our design approach. In the next section, we will apply such self-healing multiple BSW beams to simultaneously trigger an array of gold nanoantennas in a dark-field scheme, using a different device platform optimized for supporting the plasmonic response of gold in visible wavelengths.

### Far-field readout of self-healing BSW by gold nanoantennas.

For an improved plasmon resonance of the nanoantennas and far-field characterizations in this task, multilayers are designed for the visible spectrum at  $\lambda = 660$  nm. Here, the element layer is made of a 30 nm thick  $\text{Si}_3\text{N}_4$  layer. In order to preserve the refraction angle for the fraxicon, the index contrast  $\Delta n_{\text{eff}}$  of this platform is kept comparable to that of the 1555 nm platform, i.e.,  $\Delta n_{\text{eff}} = 0.1$ . However, the shortened wavelength and different effective indices (i.e.,  $n_{\text{eff}1} = 1.22$  and  $n_{\text{eff}2} = 1.12$ ) require new designs for the fraxicon. By 2D simulations, we obtain an optimal fraxicon device that conserves the refraction angle  $\theta_r$  around  $5^\circ$ . Each array of segments consists of 15 right triangles of  $w = 2$   $\mu\text{m}$  and  $h = 1.8$   $\mu\text{m}$ , leading to  $\theta_b = 42^\circ$  and a fraxicon lateral extension of 60  $\mu\text{m}$ . From the simulated intensity distribution behind this newly designed fraxicon (see Supplementary Fig. 1 and Supplementary Note 1), we can obtain the position of the self-healing BSW beams, where gold nanoantennas will be placed. Here, we employ a pair of upside-down triangles for the gap antenna. Detailed antenna design processes are presented in Supplementary Note 2, where designs of a bowtie and a pair of diamonds and upside-down triangles (see Supplementary Fig. 2) are compared while illuminated by a photonic nanojet focuser (see Supplementary Fig. 3) to monitor enhanced responses of a single antenna. Compared to the conventional bowtie antennas, the upside-down triangle pair shows better field confinement at the gap location for a wider range of the aspect ratio variations, i.e., the length  $L$  over the height  $H$  of the antenna segment (see Supplementary Fig. 4). The antenna with nominal dimensions of  $L = 140$  nm,  $H = 70$  nm, and a nominal gap of 10 nm will be placed on the position of each self-healing BSW beam. With metallic nanoantennas, even the simplified 2D simulations become more complex. Therefore, in order to acquire reasonable results, we reduce the region of interest to the first five rows of the multiple spots (see the design layout in Supplementary Fig. 5). The 2D simulation result with the antenna array confirms that the illumination self-healing beams are effectively addressing the antennas. However, since the gap size of 10 nm is too small with respect to the entire simulation space (i.e., 80  $\mu\text{m}$  by 60  $\mu\text{m}$  in the  $x$ - $z$  plane), the precise data analysis of the antenna array in such a large simulation is not feasible.

While the illuminating surface wave is evanescent and does not reach the far-field, the confined hotspot in the gap of the antenna will be scattered to all directions. Therefore, the response of the antenna array can be examined by a far-field detection without the SNOM measurements, strongly simplifying the readout of BSWs. For the experimental demonstration, we fabricate the BSW fraxicon device with the gold nanoantenna array. First, we pattern the nanoantennas and fiducial marks with a 40 nm thick gold layer on 5 nm of chromium for adhesion on top of the multilayer

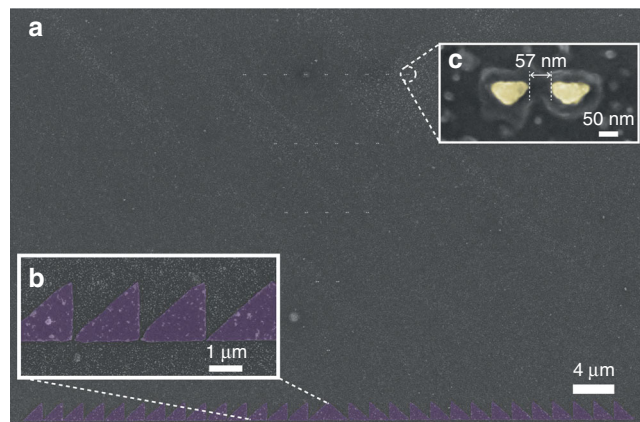


**Fig. 4** Scanning electron microscope (SEM) images of the fabricated device. The fraxicon device of 30 nm thick  $\text{Si}_3\text{N}_4$  is highlighted in violet and a nanoantenna array in yellow. **a** Entire device image. The inset in **b** shows the fraxicon and in **c** the upside-down triangle gold nanoantenna

chip by electron-beam lithography (EBL) and followed lift-off process. Those metallic fiducial marks are essential for aligning the fraxicon device with respect to the position of the antenna array in the second EBL process. Second, the patterned fraxicon in the resist layer (ma-N 2403, Micro Resist Technology GmbH) is transferred to the 30 nm thick element layer of  $\text{Si}_3\text{N}_4$  by reactive-ion etching (RIE). Details concerning the fabrication processes are described in the Methods section. Figure 4 shows a scanning electron microscope (SEM) image of a fabricated device consisting of the fraxicon device (30 nm thick  $\text{Si}_3\text{N}_4$ ) and the nanoantenna array. In order to avoid a charging effect during SEM imaging, a thin conductive layer (Espacer, Showa Denko K.K.) is spin-coated on the fabricated device.

Although the dimensions deviate from the original design (i.e.,  $L = 140$  nm,  $H = 70$  nm, and a nominal gap of 10 nm), in the gap still a relatively strong confinement is observed which can be easily detected in the far-field. In addition, the responses of the fraxicon and nanoantenna array are not significantly perturbed by minor surface imperfections, which are visible in the SEM image. For the experiment, we launch the BSW with a collimated  $\lambda = 660$  nm laser beam in the Kretschmann setup with an excitation angle of  $\theta = 50^\circ$  inside the glass prism. To cover the 60  $\mu\text{m}$  wide fraxicon device, the excitation beam has a diameter of approximately 100  $\mu\text{m}$ . The excitation position is 100  $\mu\text{m}$  behind the fraxicon. The far-field image of the simultaneously triggered antenna array is shown in Fig. 5a, which is captured by a 100x NA0.9 microscope objective and a complementary metal-oxide-semiconductor (CMOS) image sensor (Mightex Systems, 1280  $\times$  1024 pixels with pixel resolution of 5.2  $\mu\text{m}$ ). To compare with the non-self-healing illumination, we illuminate the antenna array with the propagating BSW from the other direction. Like this, the BSW does not pass the fraxicon and illuminates directly the antenna array (see the result in Fig. 5b). This non-self-healing illumination scheme shows that the responses of the antennas in the back rows are weaker than the case of the self-healing illumination in Fig. 5a. For a quantitative evaluation, we extract the mean intensity of spatial integration of 7 by 7 pixels from the antennas position in each row from Fig. 5a, b, and plot the average of each row in Fig. 5c. The extracted data were normalized to the maximum value of the average of each row. The far-field imaging relies on the capability of the objective lens and accordingly the diffraction limit is the performance barrier which smears out the sharp resonance of the antenna response. Here, our attention lies on comparing the relative response of the antennas in each row, which verifies that the self-healing BSW

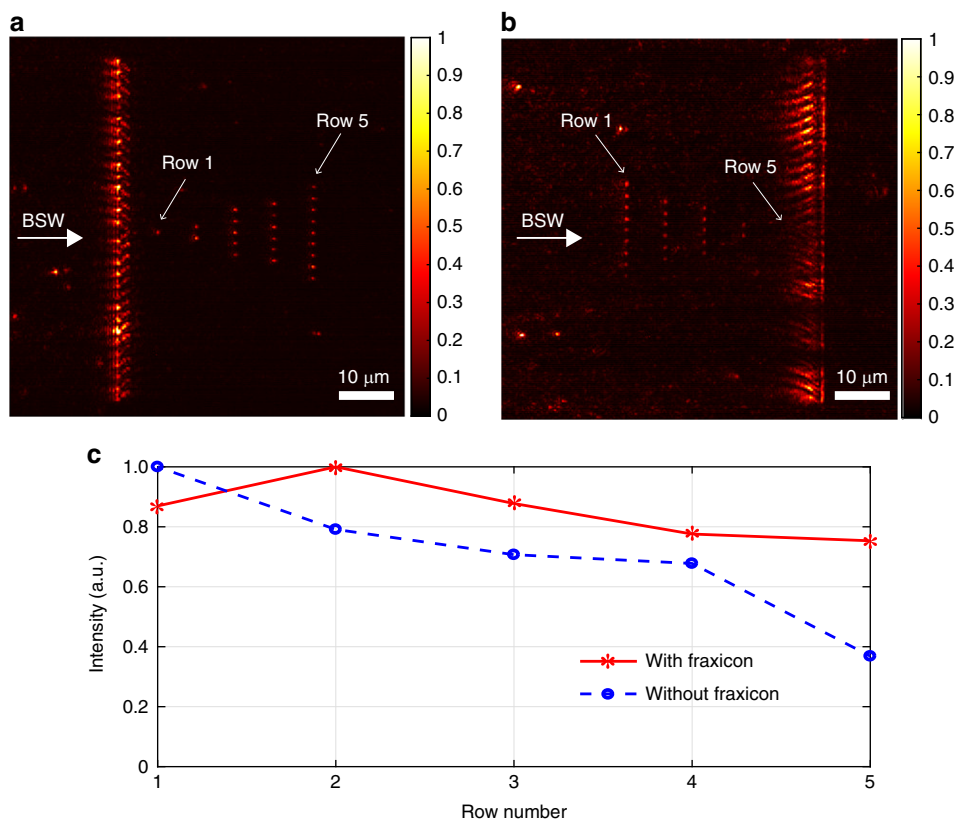


**Fig. 5** Far-field readout results. **a** The self-healing and **b** non-self-healing illuminations. The intensities are normalized in each figure. The excited Bloch surface wave (BSW) propagates from the left to the right side. Images are taken by a 100x NAO.9 objective and a complementary metal-oxide-semiconductor image sensor. **c** The mean intensity of spatial integration of 7 by 7 pixels from each antenna position is averaged for each row. The results demonstrate that the self-healing BSW beams can reach behind the obstacles, leading to comparable antenna responses for all the rows without a significant decrease of the peak intensity

beams can simultaneously deliver comparable energy to all the antennas or not. Figure 5c clearly shows that the self-healing multiple BSW beams lead to comparable responses from all the rows, while the non-self-healing illumination gradually drops the antenna response over the rows.

## Discussion

We propose and demonstrate a BSW manipulation technique which can generate multiple self-healing surface wave beams using a 2D fraxicon device. First, we investigate the response of the designed fraxicon device by near-field measurements using a custom-made SNOM at  $\lambda = 1555$  nm. The SNOM visualizes the existence of multiple self-healing BSW beams which are numerically anticipated by 2D and 3D simulations. Second, after verification of the performance of the 2D fraxicon on the BSW platform, we apply such multiple self-healing beams to simultaneously trigger an array of gold nanoantennas. This also demonstrates the hybrid integration concept combining the BSW platforms and plasmon devices. Since the visible spectrum leads to better resonance responses for the gold nanoantennas, we employ a multilayer device designed for  $\lambda = 660$  nm. A pair of upside-down triangles is used for the gap antenna design, which shows robust behavior over wider variation of the segment size. The far-field readout of the antenna response demonstrates the self-healing properties of the 2D BSW fraxicon and the dark-field illumination scheme. Compared to the case of non-self-healing illumination, all the antennas in the array are evenly illuminated by the fraxicon, showing the antennas in the back rows with strong signals. Without losing the self-healing properties, such multiple nondiffracting BSW beams can also equally illuminate

an array of dielectric scatterers distributed on the top surface of the device at the cost of weaker far-field scattering signals. This concept can be extended for more complex manipulations of the BSW using 2D diffractive optical elements and 2D meta-structures. Finally, the fabricated hybrid device of the BSW and plasmon antennas can be useful for addressing multiple nano-size specimens in the sensing and optical trapping applications.

## Methods

**Multilayer design.** Multilayers are designed for TE polarization which is parallel to the  $x$ -axis in the notation applied in this work. The multilayer design has been performed by calculating the band-gap diagram and dispersion curves using a transfer matrix method<sup>9</sup>. More details can be found in Supplementary Note 3. The beam manipulation relies on the effective refractive indices of the multilayer platform with and without the element layer. Their difference leads to the index contrast in the dispersion relation of the BSW. Here, the effective refractive index of the BSW is defined by  $n_{\text{BSW}} = c\beta/\omega$ , where  $c$  is the speed of light in vacuum,  $\omega$  the angular frequency, and  $\beta = k \sin \theta$  the propagation constant of the surface mode, with  $k$  the propagation constant in the glass substrate and  $\theta$  the incident angle in the Kretschmann configuration.

**Multilayer platform for  $\lambda$  of 1555 nm.** The multilayer stack consists of six periods of silicon nitride ( $\text{Si}_3\text{N}_4$ ,  $n_{\text{Si}_3\text{N}_4} = 1.94$ ,  $t = 283$  nm) and silicon dioxide ( $\text{SiO}_2$ ,  $n_{\text{SiO}_2} = 1.468$ ,  $t = 472$  nm) layers, where  $t$  denotes the thickness. An additional 50 nm thick layer of  $\text{Si}_3\text{N}_4$  is deposited on the periodic stack as an optional defect layer to manipulate the initial dispersion. The element layer is a 47 nm thick titanium dioxide layer ( $\text{TiO}_2$ ,  $n_{\text{TiO}_2} = 2.23$ ) which is patterned to form the fraxicon element. The total thickness of the multilayer stack is approximately 4.6 μm. The calculated band-gap diagram and dispersion curves are shown in Supplementary Fig. 6a. At the target wavelength, the reflectance curves for the multilayer platform with and without the element layer are shown in Supplementary Fig. 6b, where the position of the reflectance dip indicates the effective indices with and without the element layer,  $n_{\text{eff}1} = 1.3$  and  $n_{\text{eff}2} = 1.2$ , respectively, resulting in the index contrast  $\Delta n_{\text{eff}} = 0.1$ .

**Multilayer platform for  $\lambda$  of 660 nm.** The multilayer design for a target wavelength of 660 nm consists of four periods of silicon nitride ( $\text{Si}_3\text{N}_4$ ,  $n_{\text{Si}_3\text{N}_4} = 1.99$ ,  $t = 125$  nm) and silicon dioxide ( $\text{SiO}_2$ ,  $n_{\text{SiO}_2} = 1.475$ ,  $t = 175$  nm) layers. For this design, an additional 30 nm thick layer of  $\text{Si}_3\text{N}_4$  is used as the element layer, which is patterned to form the fraxicon element. No special defect layer has been used in this case. The total thickness of the multilayer stack is approximately 1.23  $\mu\text{m}$ . The corresponding dispersion curves and band-gap diagrams are shown in Supplementary Fig. 7a. The reflectance curves with respect to the effective index are plotted in Supplementary Fig. 7b, showing  $n_{\text{eff}1} = 1.22$  and  $n_{\text{eff}2} = 1.12$ . The effective indices of the multilayer with and without the element layer are designed to have a comparable index contrast to that of the 1555 nm platform, i.e.,  $\Delta n_{\text{eff}} = 0.1$ .

**Numerical modeling.** For rapid design variations, numerical calculations are conducted by 2D simulations which are confirmed by 3D full-wave modeling (see Supplementary Note 4) and SNOM measurements in Fig. 3. In 2D, we consider a scalar field (the magnetic field component in  $y$ -direction) to propagate in the  $x$ - $z$  plane of a medium characterized by the spatial distribution of the effective refractive index according to the spatial distribution of the patterned element layer. This simplification is similar to a comparable method for waveguide systems<sup>43</sup>. Consequently, the multilayer stack is not included in those 2D simulations, in contrast to 3D full-wave simulations. This 2D model mimics the propagation of the BSW along the surface. For the final design of the fraxicon, full 3D simulations considering the exact geometry including the multilayer stack are performed to verify the 2D simulation results. For more information, please refer to the details in Supplementary Note 4 and the simulation result of the 3D modeling in Supplementary Fig. 8. All simulations have been performed using a time domain solver in CST Microwave Studio which is based on the finite integration technique. We emphasize the fact that even though demonstrated here at specific operational wavelengths, i.e.,  $\lambda = 660$  nm and 1555 nm, the scalability of Maxwell's equations allows to extrapolate all observed effects to different spectral regions, as long as materials with suitable dielectric properties are available.

**Fabrication of 1555 nm platform.** For the multilayer platform, six periods of  $\text{Si}_3\text{N}_4$  and  $\text{SiO}_2$  are alternately deposited on a fused silica substrate using plasma-enhanced chemical vapor deposition (PECVD, PlasmaLab 80 Plus by Oxford). An additional 50 nm thick layer of  $\text{Si}_3\text{N}_4$  is deposited as the defect layer. Used precursor gases are silane ( $\text{SiH}_4$ ), ammonia ( $\text{NH}_3$ ), and nitrous oxide ( $\text{N}_2\text{O}$ ), and the process temperature is 300 °C.

For the element layer, the 47 nm thick layer of  $\text{TiO}_2$  was deposited by atomic layer deposition (ALD)<sup>44</sup>. The low deposition rate (0.069 nm/cycle) and the conformity of the ALD technique are well known for providing a great control of the film thickness and the generation of outstanding homogeneous layers<sup>45</sup>. The two precursors used in the  $\text{TiO}_2$  deposition process are titanium tetrachloride ( $\text{TiCl}_4$ ) and water ( $\text{H}_2\text{O}$ ), and the process temperature is 120 °C.

The patterning of this  $\text{TiO}_2$  element layer was performed by EBL (Vistec EBPG 5000+ ES HR). A chromium (Cr) layer was first evaporated (LAB18, Kurt J. Lesker) and a resist (hydrogen silesquioxane (HSQ)) layer was spun on the sample. The resist was then exposed to the electron beam for the writing of the geometry, and developed using a solution of AZ 351: $\text{H}_2\text{O}$  (1:3) developer. The geometry is then transferred to the Cr layer by inductively coupled plasma reactive-ion etching process (ICP-RIE, PlasmaLab 100 by Oxford) under chlorine (Cl) and oxygen ( $\text{O}_2$ ) gases. The structure is finally transferred to  $\text{TiO}_2$  element layer by a second etching step (ICP-RIE under  $\text{SF}_6$  and argon, PlasmaLab 80 by Oxford). The remaining Cr was removed by wet etching.

**Fabrication of 660 nm platform with gold nanoantennas.** For the multilayer platform, four periods of  $\text{Si}_3\text{N}_4$  and  $\text{SiO}_2$  are alternately deposited on a fused silica substrate using PECVD (PlasmaLab 80 Plus by Oxford). An additional 30 nm thick layer of  $\text{Si}_3\text{N}_4$  is deposited as the element layer which is different from the previous section, where  $\text{TiO}_2$  is the element layer. Used precursor gases are silane ( $\text{SiH}_4$ ), ammonia ( $\text{NH}_3$ ), and nitrous oxide ( $\text{N}_2\text{O}$ ), and the process temperature is 300 °C.

Prior to the patterning of the  $\text{Si}_3\text{N}_4$  element layer, we pattern the gold nanoantenna and fiducial marks with a 40 nm thick gold layer on 5 nm of chromium for adhesion on top of the multilayer chip. For this gold layer patterning, we use a two-layer PMMA (poly(methyl methacrylate)) resist system (PMMA 600 K (2%) AR-P 662.04 and PMMA 950 K (2.25%) AR-P 672.045) with a total thickness of around 120 nm. To avoid charging of the dielectric samples during the EBL process, a conductive polymer (Spacer, Showa Denko K.K.) is spun on the sample which renders the conductivity for the dielectric materials. After the PMMA resist patterning, we deposit 5 nm chromium and 40 nm gold in a thermal evaporator for a subsequent lift-off step in acetone. For the  $\text{Si}_3\text{N}_4$  layer patterning, we use ma-N 2403 (negative electron-beam resist,  $t = 340$  nm) together with an adhesion promoter (TI Prime). Spacer is applied on the sample to avoid charging of the dielectric layer during the EBL. Developed patterns of ma-N 2403 are transferred to the  $\text{Si}_3\text{N}_4$  layer by plasma etching (Oxford RIE 80):  $\text{CHF}_3 + \text{O}_2$  RIE plasma for 30 s with the etch rate of  $\text{Si}_3\text{N}_4 = 1$  nm/s. Subsequently, the remaining resist is removed by  $\text{O}_2$  plasma.

## Data availability

The data that support the findings of this study are available from the corresponding author upon reasonable request.

Received: 7 May 2018 Accepted: 10 September 2018

Published online: 03 October 2018

## References

- Fang, Y. & Sun, M. Nanoplasmonic waveguides: towards applications in integrated nanophotonic circuits. *Light Sci. Appl.* **4**, e294 (2015).
- Du, W., Wang, T., Chu, H. S. & Nijhuis, C. A. Highly efficient on-chip direct electronic plasmonic transducers. *Nat. Photonics* **11**, 623–627 (2017).
- Chang, C. W., Lin, C. E., Yu, C. J., Yeh, T. T. & Yen, T. J. Miniature surface plasmon polariton amplitude modulator by beat frequency and polarization control. *Sci. Rep.* **6**, 32098 (2016).
- Vest, B. et al. Anti-coalescence of bosons on a lossy beam splitter. *Science* **356**, 1373–1376 (2017).
- Fang, Z., Lin, F., Huang, S., Song, W. & Zhu, X. Focusing surface plasmon polariton trapping of colloidal particles. *Appl. Phys. Lett.* **94**, 063306 (2009).
- Tan, Q., Roussey, M., Cosentino, A. & Herzig, H. P. In-plane illuminated metallic annular aperture array for sensing application. *Opt. Lett.* **37**, 635–637 (2012).
- Raether, H. *Surface Plasmons on Smooth and Rough Surfaces and on Gratings* (Springer, New York, 1988).
- Berini, P. Long-range surface plasmon polaritons. *Adv. Opt. Photonics* **1**, 484–588 (2009).
- Yeh, P., Yariv, A. & Hong, C. S. Electromagnetic propagation in periodic stratified media. I. General theory. *J. Opt. Soc. Am.* **67**, 423–438 (1977).
- Kretschmann, E. & Raether, H. Radiative decay of nonradiative surface plasmons excited by light. *Z. Naturforsch. A* **23**, 2135–2136 (1968).
- Descrovi, E. et al. Leakage radiation interference microscopy. *Opt. Lett.* **38**, 3374–3376 (2013).
- Angelini, A. et al. Focusing and extraction of light mediated by Bloch surface waves. *Sci. Rep.* **4**, 5428 (2014).
- Dubey, R. et al. Experimental investigation of the propagation properties of Bloch surface waves on dielectric multilayer platform. *J. Eur. Opt. Soc. Rapid Publ.* **13**, 5 (2017).
- Yu, L., Barakat, E., Di Francesco, J. & Herzig, H. P. Two-dimensional polymer grating and prism on Bloch surface waves platform. *Opt. Express* **23**, 31640–31647 (2015).
- Sfez, T. et al. Two-dimensional optics on silicon nitride multilayer: refraction of Bloch surface waves. *Appl. Phys. Lett.* **96**, 151101 (2010).
- Descrovi, E. et al. Guided Bloch surface waves on ultrathin polymeric ridges. *Nano Lett.* **10**, 2087–2091 (2010).
- Yu, L., Barakat, E., Nakagawa, W. & Herzig, H. P. Investigation of ultra-thin waveguide arrays on a Bloch surface wave platform. *J. Opt. Soc. Am. B* **31**, 2996–3000 (2014).
- Yu, L. et al. Manipulating Bloch surface waves in 2D: a platform concept-based flat lens. *Light Sci. Appl.* **3**, e124 (2014).
- Kim, M.-S. et al. Subwavelength focusing of Bloch surface wave. *ACS Photonics* **4**, 1477–1483 (2017).
- Smolik, G. M., Deschermes, N. & Herzig, H. P. Toward Bloch surface wave-assisted spectroscopy in the mid-infrared region. *ACS Photonics* **5**, 1164–1170 (2018).
- Kovalevich, T. et al. Polarization controlled directional propagation of Bloch surface wave. *Opt. Express* **25**, 5710–5715 (2017).
- Menotti, M. & Liscidini, M. Optical resonators based on Bloch surface waves. *J. Opt. Soc. Am. B* **32**, 431–438 (2015).
- Dubey, R. et al. Near-field characterization of a Bloch-surface-wave-based 2D disk resonator. *Opt. Lett.* **41**, 4867–4870 (2016).
- Vosoughi Lahijani, B. et al. Experimental demonstration of critical coupling of whispering gallery mode cavities on Bloch surface wave platform. *Opt. Lett.* **42**, 5137–5140 (2017).
- Kim, M.-S., Vosoughi Lahijani, B. & Herzig, H. P. Stepwise Luneburg lens for Bloch surface waves. *Appl. Sci.* **8**, 245 (2018).
- Wang, R. et al. Bloch surface waves confined in one dimension with a single polymeric nanofiber. *Nat. Commun.* **8**, 14330 (2017).
- Lerario, G. et al. High-speed flow of interacting organic polaritons. *Light Sci. Appl.* **6**, e16212 (2017).
- Lerario, G. et al. Room temperature Bloch surface wave polaritons. *Opt. Lett.* **39**, 2068–2071 (2014).
- Wang, M. et al. Magnetic spin-orbit interaction of light. *Light Sci. Appl.* **7**, 24 (2018).
- Santi, S. et al. Real-time amyloid aggregation monitoring with a photonic crystal-based approach. *Chemphyschem* **14**, 3476–3482 (2013).

31. Rizzo, R. et al. Bloch surface wave enhanced biosensor for the direct detection of angiotensin-2 tumor biomarker in human plasma. *Biomed. Opt. Express* **9**, 529–542 (2018).
32. Lereu, A. L., Zerrad, M., Passian, A. & Amra, C. Surface plasmons and Bloch surface waves: towards optimized ultra-sensitive optical sensors. *Appl. Phys. Lett.* **111**, 011107 (2017).
33. Koju, V. & Robertson, W. M. Leaky Bloch-like surface waves in the radiation-continuum for sensitivity enhanced biosensors via azimuthal interrogation. *Sci. Rep.* **7**, 3233 (2017).
34. Zhang, D. et al. Extending the propagation distance of a silver nanowire plasmonic waveguide with a dielectric multilayer substrate. *Nano Lett.* **18**, 1152–1158 (2018).
35. Xiang, Y. et al. Manipulating propagation constants of silver nanowire plasmonic waveguide modes using a dielectric multilayer substrate. *Appl. Sci.* **8**, 144 (2018).
36. Durnin, J., Miceli, J. J. Jr. & Eberly, J. H. Diffraction-free beams. *Phys. Rev. Lett.* **58**, 1499–1501 (1987).
37. Lin, J. et al. Cosine-Gauss plasmon beam: a localized long-range nondiffracting surface wave. *Phys. Rev. Lett.* **109**, 093904 (2012).
38. Wang, R. et al. Diffraction-free Bloch surface waves. *ACS Nano* **11**, 5383–5390 (2017).
39. Garcia-Ortiz, C. E., Coello, V., Han, Z. & Bozhevolnyi, S. I. Generation of diffraction-free plasmonic beams with one-dimensional Bessel profiles. *Opt. Lett.* **38**, 905–907 (2013).
40. Shi, W. B., Chen, T. Y., Jing, H., Peng, R. W. & Wang, M. Dielectric lens guides in-plane propagation of surface plasmon polaritons. *Opt. Express* **25**, 5772–5780 (2017).
41. McLeod, J. H. The axicon: a new type of optical element. *J. Opt. Soc. Am.* **44**, 592–597 (1954).
42. Golub, I. Fresnel axicon. *Opt. Lett.* **31**, 1890–1892 (2006).
43. Knox, R. M. & Toullos, P. P. Integrated circuits for the millimeter through optical frequency range. in *Proc. Symp. Submillimeter Waves*, 497–516 (Polytechnic Press of Polytechnic Institute of Brooklyn, New York, 1970).
44. Leskelä, M. & Ritala, M. Atomic layer deposition (ALD): from precursor to thin film structures. *Thin. Solid. Films.* **409**, 138–146 (2002).
45. Häyrynen, M., Roussey, M., Bera, A., Kuittinen, M. & Honkanen, S. Atomic Layer Re-Deposition for Nanoscale Devices. (ed. Leon Shohet, J.) in *Encyclopedia of Plasma Technology*, 143–151 (Taylor & Francis Group, New York, 2017).

## Acknowledgements

This research is supported by the Finnish Funding Agency for Innovation (Tekes) FiDiPro NP-NANO (40315/13) and funding from the European Union's Horizon 2020

research and innovation programme under the Marie Skłodowska-Curie grant agreement no. 675745. A.V. acknowledges support from the Karlsruhe School of Optics and Photonics (KSOP). The authors want to thank S. Diewald, N. Gruhler, J. Straubel, and F. Negrodo for useful discussions and technical support.

## Author contributions

M.-S.K. conceived the project and experiments. M.H., M.K., and M.R. contributed on ALD deposition and patterning the fraxicon element. A.V. fabricated nanoantennas and the corresponding multilayer device. M.-S.K. and A.V. performed the 2D and 3D simulations, respectively. B.V.L. conducted the SNOM measurements. M.-S.K., A.V., and C.R. analyzed the experimental results and data and wrote the manuscript. H.P.H. supervised the research.

## Additional information

**Supplementary information** accompanies this paper at <https://doi.org/10.1038/s42005-018-0065-9>.

**Competing interests:** The authors declare no competing interests.

**Reprints and permission** information is available online at <http://npg.nature.com/reprintsandpermissions/>

**Publisher's note:** Springer Nature remains neutral with regard to jurisdictional claims in published maps and institutional affiliations.



**Open Access** This article is licensed under a Creative Commons Attribution 4.0 International License, which permits use, sharing, adaptation, distribution and reproduction in any medium or format, as long as you give appropriate credit to the original author(s) and the source, provide a link to the Creative Commons license, and indicate if changes were made. The images or other third party material in this article are included in the article's Creative Commons license, unless indicated otherwise in a credit line to the material. If material is not included in the article's Creative Commons license and your intended use is not permitted by statutory regulation or exceeds the permitted use, you will need to obtain permission directly from the copyright holder. To view a copy of this license, visit <http://creativecommons.org/licenses/by/4.0/>.

© The Author(s) 2018